Results in Physics 15 (2019) 102564

Contents lists available at ScienceDirect

Results in Physics

journal homepage: www.elsevier.com/locate/rinp

Hierarchiral 4-tetranitro copper(II)phthalocyanine based metal organic framework hybrid composite with improved electrocatalytic efficiency towards hydrogen evolution reaction

Gobeng Release Monama[a,b], Mpitloane Joseph Hato[a,c,*], Kabelo Edmond Ramohlola[a], Thabiso Carol Maponya[a], Siyabonga Beizel Mdluli[b], Kerileng Mildred Molapo[b], Kwena Desmond Modibane[a,*], Emmanuel I. Iwuoha[b], Katlego Makgopa[d], Malesela Daniel Teffu[a]

[a] Nanotechnology Research Lab, Department of Chemistry, School of Physical and Mineral Sciences, University of Limpopo (Turfloop), Sovenga 0727, Polokwane, South Africa

[b] SensorLab, Chemistry Department, University of the Western Cape, Bellville 7535, Cape Town, South Africa

[c] Department of Environmental Sciences, College of Agriculture and Environmental Sciences, University of South Africa (UNISA), Florida Science Campus, Johannesburg 1710, South Africa

[d] Department of Chemistry, Faculty of Science, Tshwane University of Technology (Acardia Campus), Pretoria 0001, South Africa

ARTICLE INFO

Keywords:
Copper(II)phthalocyanine
Composite
Electrocatalysis
Hydrogen evolution reaction
Tafel parameters

ABSTRACT

A novel hybrid-hybrid nanocomposite based on 4-tetranitro copper(II)phthalocyanine (TNCuPc) grown on metal organic frameworks (MOF) as a noble metal-free catalyst for hydrogen evolution reaction (HER) was developed by a simple impregnation method. The structure, surface area and the morphology of the bare MOF, TNCuPc and the TNCuPc/MOF composite were characterized by X-ray diffraction, Fourier transform infrared spectroscopy, ultraviolet-visible spectroscopy, Brunauer-Emmet-Teller, scanning electron microscopy, transmission electron microscopy and simultaneous thermal analysis. The electrocatalytic activity of the samples towards the HER was evaluated using electrochemical impedance spectroscopy (EIS) and cyclic voltammetry, exchange current density, i_0, Tafel slope value, b, as well as charge transfer coefficient, α. The spectroscopic analyses indicated a successful synthesis of TNCuPc and its composite. The morphological results showed the development of rod-like structures of TNCuPc on the surface of the MOF. The composite exhibited an onset potential of about −0.713 V vs. Ag/AgCl in 0.1 M TBAP/DMSO and 0.3 M H_2SO_4 solutions, which is 44 mV and 9 mV more positive than that of MOF and TNCuPc respectively. The composite showed the rate determining step (RDS) to be the Volmer reaction in conjunction with either Heyrovsky or Tafel reaction as the RDS due to the Tafel slope value of 147 mV/dec and an α of 0.4. The i_0 value of the TNCuPc/MOF composite was about 1.6 times that of the bare MOF. The EIS results showed the charge transfer resistance (R_{ct}) of 12.6 kΩ for the TNCuPc/MOF composite as compared to MOF and TNCuPc values of 41 and 18.6 kΩ, respectively, demonstrating an excellent conductivity of the composite. In addition, R_{ct} values of materials follow the sequence, blank < MOF < TNCuPc < TNCuPc/MOF. The fabricated composite displayed high activity towards the HER, high thermal stability, and excellent tolerance. Therefore, TNCuPc/MOF non-noble electrocatalyst can be a promising electrochemical catalyst to replace Pt-based catalysts for electrochemical hydrogen production.

Introduction

Recently, there has been an immense academic interest and technological development effort directed towards establishing essential basic knowledge of the hydrogen evolution reaction (HER) [1,2]. The development of new materials is needed for improved efficiency of the HER process in acidic and alkaline environments [3–5]. Currently, Pt- and Pd-based catalysts exhibit the best HER electrocatalytic performance in acid media [6,7]. Nonetheless, the cost of and scarcity of platinum group metal (PGM) catalysts make them impractical choices. Therefore, in pursuit of finding inexpensive Pt free electrocatalysts for practical applications is indeed an active area of research [8,9].

* Corresponding authors at: Nanotechnology Research Lab, Department of Chemistry, School of Physical and Mineral Sciences, University of Limpopo (Turfloop), Sovenga 0727, Polokwane, South Africa (M.J. Hato).

E-mail addresses: mpitloane.hato@ul.ac.za (M.J. Hato), kwena.modibane@ul.ac.za (K.D. Modibane).

https://doi.org/10.1016/j.rinp.2019.102564
Received 22 April 2019; Received in revised form 19 July 2019; Accepted 2 August 2019
Available online 09 August 2019

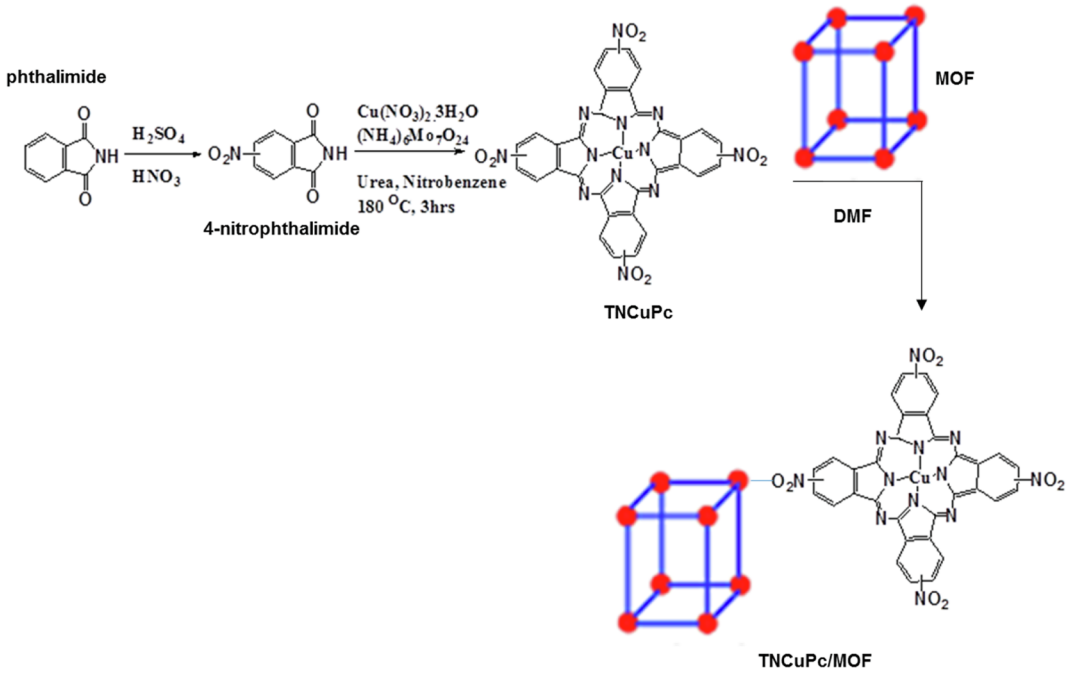

Scheme 1. Synthesis of TNCuPc/MOF composite through impregnation procedure of TNCuPc and MOF in DMF.

Recently, transition metal sulfides (MoS_2) [3], have been intensively investigated as HER catalysts due to their fascinating properties such as conductivity and good durability, whereas the basal planes exhibited poor activity [10,11].

A quite number of porous structures such as activated carbons, graphite nanofibers, metal organic frameworks (MOFs), carbon nanotubes and zeolites were considered as possible materials for HER [1,3,9,12,13]. Among these materials, MOFs have emerged as promising class of porous species in developing advanced multifunctional systems in the last two decades owing to their special structures [14]. MOFs are regarded as highly crystalline materials made up of metal ions/clusters and organic ligands due to coordination bonding. These highly crystalline materials possess high porosity, high surface area and even nanoscale cavities [15]. Therefore, these materials have received an immense attention in different applications including energy storage, CO_2 adsorption, hydrocarbon adsorption/separation, and others [16,17]. Nonetheless, application of single-component MOFs as HER catalyst has drawbacks owing to their poor electronic conductance, moisture instability, and poor H_2 adsorption/desorption at ambient conditions [17–19]. Hence, the combination of MOFs with other highly conductive inorganic semiconductors may be an ideal method to overcome those challenges. In addition, integration of electron-donating/withdrawing groups in the ligands develops the establishment of donor-acceptor structures in the MOFs and therefore adjusts electron orbital energy level of the electrochemical based devices [14].

On the other hand, tetranitro copper(II)phthalocyanine (TNCuPc) falls in the group of the metallophthalocyanine family posessing excellent redox chemistries, conjugated system of 18 electrons, chemical and good thermal stability. Thus, metallophthalocyanine can be used in many industrial applications such as in electrocatalysis, supercapacitors and sensing [15,20]. In addition, the substituents placed on the phthalocyanine ring can provide good solubility of the compound in many solvents and supramolecular organisation can also be achieved [16]. For example, tetra-substituted phthalocyanine can offer higher stability than octa-substituted phthalocyanine counter parts [21,22]. The electronic effect of the nitro groups can tune the properties of metallophthalocyanine to a higher degree than the symmetry-lowing approach [23]. Therefore, combining the remarkable properties of MOFs with functionalised phthalocyanine could be a promising path for preparing suitable electrocatalyst for HER process. The combination of MOF with TNCuPc can enhance the conductivity of the resultant composite thereby resulting to a better performance of the prepared electrochemical electrode. In this study, the Cu-MOF (HKUST-1) was fabricated by hydrothermal method, which can allow the control of size and shape, shape distribution, crystallinity, efficient synthetic conditions and possibility to control its morphological characteristics [18]. The TNCuPc/MOF composite was prepared by a modest impregnation route. Therefore, we report on the hybrid composite of TNCuPc and MOF for application as an efficient electrocatalyst for HER. It is clearly shown that this TNCuPc/MOF based electrocatalyst, as reported in the literature, can reversibly deliver good electrocatalytic HER performance in acidic medium.

Experimental details

Materials

Trimesic acid (H_3BTC), copper nitrate trihydrate ($Cu(NO_3)_2{\cdot}3H_2O$) and tetrabutylammonium percholate (TBAP) were procured from Sigma Aldrich, South Africa. Hydrochloric acid (HCl), methanol, ethanol, phthalimide, nitrobenzene, dimethyl sulfoxide (DMSO), dimethylformamide (DMF), nitric acid (HNO_3) and sulphuric acid (H_2SO_4) were bought from Rochelle Chemicals, South Africa. Urea (CH_4N_2O) and ammonium heptamolybdate ($(NH_4)_6Mo_7O_{24}$) were procured from uniLAB, South Africa.

Materials synthesis

The synthesis of 4-nitrophalimide was synthesized from reported procedure [15]. TNCuPc was prepared from 4-nitrophthalimide according to the previous work by Modibane and Nyokong with a slight modification [17]. In brief, about 3.00 g 4-nitrophthalimide in the presence of 3.00 g CH_4N_2O, 0.0800 g $NH_4)_6Mo_7O_{24}$ and 1.40 g Cu $(NO_3)_2{\cdot}3H_2O$ mixture in 15.00 mL nitrobenzene was refluxed for few hours at 180 °C. The product was washed with ethanol and dried at 110 °C and obtained a yield of 2.64 g (70%) and melting point > 300 °C.

TNCuPc/MOF composite (Scheme 1) was prepared by a direct

mixing of TNCuPc and MOF. In brief, 0.1 g of MOF (dehydrated at 150 °C for 1 h) was suspended in DMF (10 mL) and 1.4 mL of TNCuPc (0.12 mol.L^{-1}) in DMF was added. The resultant mixture was stirred for 24 h at 25 °C controlled by thermostat. The filtration was used to recover the product and washed with ethanol and then dried at 50 °C for overnight obtaining a yield of 0.09 g (92%) and melting point > 300 °C.

Spectroscopic characterizations

FTIR spectra of synthesized samples were carried out using Spectrum II spectrometer (PerkinElmer) recorded from 400 and 4000 cm^{-1} with a minimum of 32 scans and resolution of 4 cm^{-1} at room temperature. UV–vis spectra of the prepared materials in 2 ppm H_2SO_4 were obtained by means of a Varian Cary 300 UV–Vis-NIR spectrophotometer in the wavelength region between 200 and 900 nm and 1 cm optical path length quartz cuvette at room temperature. The crystallinity and structures of MOF, TNCuPc and TNCuPc/MOF composite were analyzed using X-ray diffraction (XRD Phillips PW 1830, CuK_α radiation, $\lambda = 1.5406$ A).

SEM/EDS and TEM

Surface morphology was accomplished using field-emission scanning electron microscope (FE-SEM, Auriga® Carl Zeiss) conducted at a voltage of 30 kV. The FE-SEM was coupled with elemental analyzer, energy dispersive spectroscopy (EDS). Transmission electron microscopy (TEM) analysis was performed using FEI Tecnai G2 20 transmission electron microscope at 200 kV.

HR-TEM/EDX and SAED

High resolution-transmission electron microscopy (HR-TEM) investigation was made by using FEI Tecnai G2 20 TEM coupled with electron diffraction X-ray (EDX) to study the internal morphology of the prepared materials. Energy dispersive X-ray spectra were collected using an EDAX liquid nitrogen cooled lithium doped silicon detector. The crystal structure formation of the samples was analyzed by employing the selected area electron diffraction (SAED).

STA

The stability of the samples was evaluated by means of a simultaneous thermal analyzer (STA) Perkin-Elmer 6000 instrument coupled with a PolyScience digital temperature controller under N_2 gas purged at 20 mL/min flow rate by using aluminium (melting point = 660 °C) and indium (melting point = 156.6 °C) to calibrate the system. Samples with the weight ranging from 1 to 4 mg were subjected to the heating temperature (30–500 °C) and constant heating rate (20 °C/min), and the data was analyzed using Pyris software®.

BET

Low-pressure nitrogen (77 K) adsorption isotherms were performed using an ASAP2020 instrument (Micromeritics). Approximately, 300 mg of MOF and composites were heated to 180 °C with a rate of 2 °C.min^{-1} and outgassed at 180 °C for 24 h.

CV

Cyclic voltammetry (CV) analysis was carried out in 10 mL of 0.1 M TBAP/DMSO electrolytic system using three electrode EPSILON electrochemical workstation. A gold electrode (Au) with a surface area of 0.07 cm^2 area was employed as a working electrode, while silver/silver chloride (Ag/AgCl) and platinum (Pt) wire were used as reference electrode and counter electrode, respectively. Repetitive scanning solutions of TNCuPc, MOF and TNCuPc/MOF composite ($\sim 2.0 \times 10^{-4}$ mol.L^{-1}) was ranging from −2.0 to 1.25 V at scan rates of 0.02–0.10 Vs^{-1}. HER measurements were done using varying the concentration of H_2SO_4 from 0.03 to 0.45 M as a hydrogen source in 0.1 M TBAP/DMSO system and $\sim 2.0 \times 10^{-4}$ mol.L^{-1} of MOF, TNCuPc and TNCuPc/MOF as potential electrochemical catalysts.

EIS

The electrochemical impedance spectroscopy (EIS) measurements for MOF, TNCuPc and TNCuPc/MOF composite were performed with the frequency ranging from 5.0×10^5 Hz − 0.7 Hz in 0.1 M TBAP/DMSO electrolyte at open circuit potential (OCP). To guarantee the reproducibility of the experimental data, all measurements were carried out in triplicate.

Results and discussion

Characterization of the as-synthesized MOF, TNCuPc and TNCuPc/MOF samples

The UV absorption spectra of synthesized materials (MOF, TNCuPc and TNCuPc/MOF composite) in a concentrated H_2SO_4 are shown in Fig. 1(a). MOF shows no absorption in the visible region owing to poor stability of the MOF material in acidic condition [21]. The spectra for TNCuPc and TNCuPc/MOF composite showed an intense Q absorption band between 720 and 780 nm in the visible range and a B band between 300 and 400 nm in the UV region. Both Q and B bands result from to π-π* transitions originating from the Pc ligand. The Q-band is assigned to the 6eg → 2a1u transition while the B band is attributable to 6eg → 4a2u [24]. The maximum wavelength values of the Q band for the TNCuPc and its composite are in accordance with the work reported by Cong et al. [24]. These observations indicate the presence of phthalocyanine in the composite. The Q band of the TNCuPc and composite was broad, split and shifted slightly to blue-region [24–26]. The broadening and the unusual Q band split may be attributed to the effect of the solvent used in this study. Furthermore, after the incorporation of TNCuPc and MOF, there was a blue shift in absorption peaks confirming formation of TNCuPc/MOF composite. This typical behaviour of blue shift of absorption was observed after the phthalocyanine were doped with the Fe_3O_4 nanoparticles [22].

To confirm the formation of the TNCuPc/MOF composite, FTIR (Fig. 1b) was employed in the region between 500 and 4500 cm^{-1}. The peaks in the 3430–3000 cm^{-1} region for MOF are due to OH and C–H aromatic bands of the organic linker coordinated to the copper sites [18,23]. The most intense peaks at 1374 cm^{-1} and 1647 cm^{-1} are due to C–O symmetric and C = O asymmetric stretching vibrations of the carboxylate groups in H_3BTC, respectively [23,27]. The bands at 1646 cm^{-1} resulted from aromatic C = C and 1718 cm^{-1} from COO − of H_3BTC [28,29]. The peaks for the N–H and C = O vibrations in the IR spectrum of 4-nitrophthalimide at ~3283 and 1720 cm^{-1} [30], respectively, disappeared after conversion into TNCuPc as an indicative of metallophthalocyanine formation [31]. The vibrational peaks between 700 and 900 cm^{-1} are typically the results of phthalocyanines skeletal vibrations [32]. The characteristic of NO_2 stretch was observed at around 1350 and 1450 cm^{-1}, which is a substituent in the prepared TNCuPc. As shown in Fig. 1b, all intense bands between 1350 and 1650 cm^{-1} were attributed to phenyl modes in MOF and CuPc structures as a confirmation of TNCuPc/MOF composite synthesis. A slight shift in the maximum of this band suggests the formation of π-π interaction between the MOF and the phthalocyanine. However, the changes in the environment of the carboxylate ligands which are likely related to the distortion of the MOF structure owing to the introduction of TNCuPc and the interaction of the ligands with the Pc. These are seen from the variations in the ratios of the bands between 1350 and 1650 cm^{-1}. Furthermore, there is a new signal developed at 489 cm^{-1} for TNCuPc/MOF composite, which clearly suggests a successful

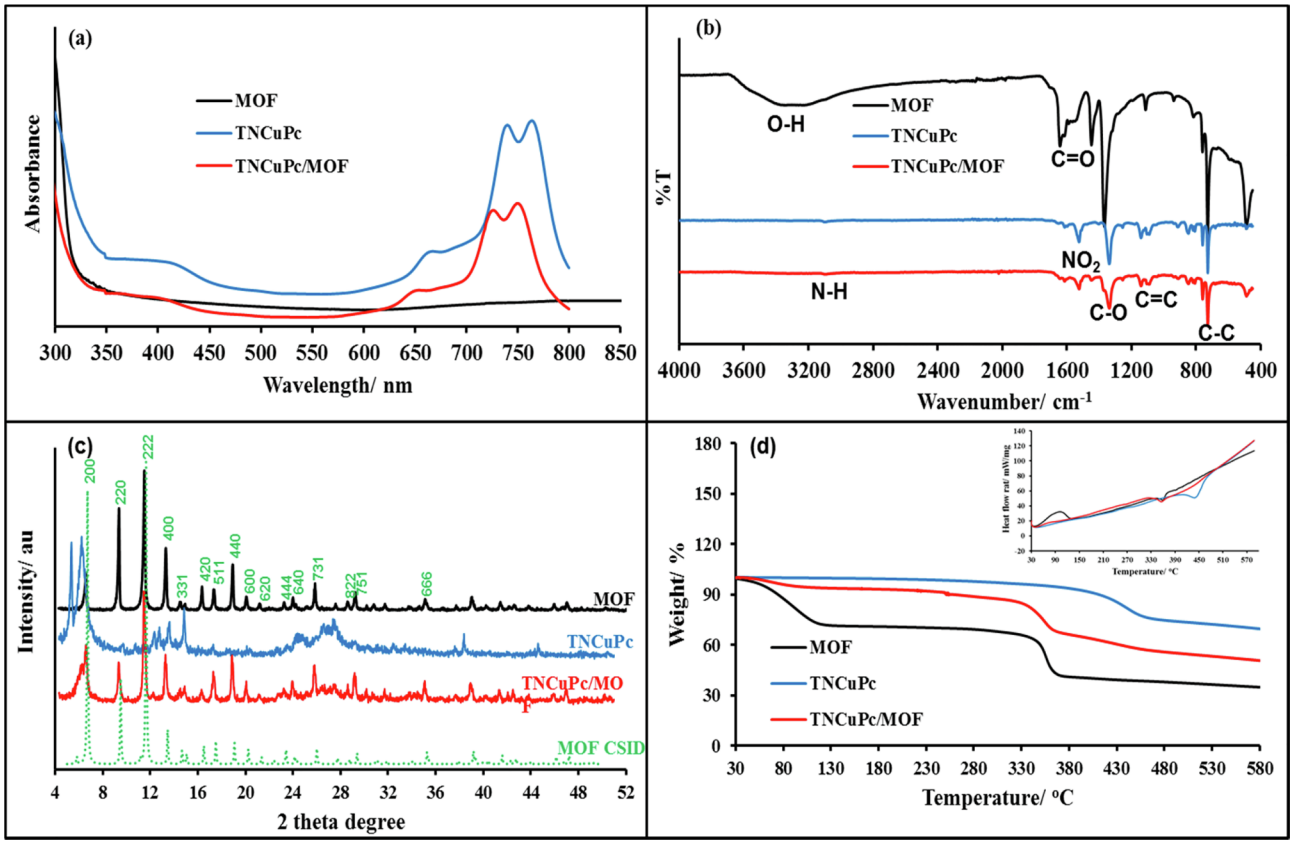

Fig. 1. (a) UV–vis; (b) FTIR; (c) XRD spectra; and (d) TGA results of MOF, TNCuPc and TNCuPc/MOF composite (inset: DSC thermograms).

preparation of the composite. This band is not observable when the TNCuPc was formed and is due to the stretching vibrations of − C = C bonds in MOF rings.

Fig. 1c shows the XRD patterns of MOF crystal structural information data (CSID), MOF, TNCuPc and TNCuPc/MOF composite. It can be seen that all the peaks of MOF are similar to those reported by Ramohlola et al. [33] with good crystallinity similar to the crystal structure simulated data (CSID). The patterns shown in this figure for MOF appear at lower 2θ angles possess micro-porous structure characteristic [34]. In addition, they possess a number tiny pores or cavities which are in good agreement with a typical structure of MOF [35–37]. The most intense peaks on the diffraction pattern of TNCuPc appearing at 2θ = 5.7, 6.9 and 9.1° correspond to miller indices (1 0 0), (1 1 0) and (1 1 1), respectively All other peaks located at 2θ = 13, 14.5 and 27.2° are attributed to the diffraction peaks of TNCuPc [38,39]. Notably, the 2θ angle around 28° in the diffraction peaks of the TNCuPc was broader and weak, indicating large crystal sizes or poor crystallinity of TNCuPc [38]. Previous studies have reported similar patterns, which suggest a cubic phthalocyanine structure [24,28]. In the case of TNCuPc/MOF composite, the main peaks appearing at 2θ = 6.97° are associated to (1 1 0) reflection of TNCuPc and 2θ = 12° accounts for the reflection (2 2 2) of MOF phase. It should be noted that the intensity of the broad peak appearing at 2θ = 28° for TNCuPc decreases in the composite, which suggests a successful preparation of the TNCuPc/MOF. Furthermore, a number of sharp peaks are observed suggesting highly crystalline phases of MOF were maintained, therefore, the presence of TNCuPc does not inhibit the formation of linkages between Cu dimers and organic bridges [40].

Thermogravimetric analysis (TGA) was employed to investigate the thermal stability of the synthesized MOF, TNCuPc and the MOF/TNCuPc composite and also to determine the composition of the prepared TNCuPc/MOF composite and the results are presented in Fig. 1d. As observed in the TGA curve of MOF, the degradation step between 35 and 125 °C was due to the evaporation of water and also some organic contaminants [41]. It is noticeable that MOF and TNCuPc/MOF composite show two similar thermogravimetic degradation steps over the experimental temperature range investigated. The two degradation steps are seen at around 100 and 325 °C. These steps are normally associated to the intrinsic thermal degradation behaviors of MOF corresponding to water molecules and ethanol physisorbed in the framework of MOF by losing its organic linker molecules and leaving the CuO [29,40-43]. The TGA profiles of MOF agreed very well with those reported by our recent work [18]. The MOF exhibits an overall weight loss of 60%, while both TNCuPc and TNCuPc/MOF composite show 20 and 40%, respectively. TNCuPc exhibits good thermal stability typically for Pcs [20] and one degradation step at around 400 °C, corresponding to the oxidative degradation of TNCuPc [32]. At the initial step, the small weight loss in TNCuPc/MOF composite is owing to the release of water molecules and the removal of some organic contaminants, including the evaporation of guest molecules from the pores such as ethanol [29]. When TNCuPc is introduced in MOF, the stability of the composite was increased as compared to bare MOF. This may be attributed to a strong π-π interaction between TNCuPc and MOF as observed in FTIR by a development of new band. The inset in Fig. 1d demonstrates DSC curves of MOF, TNCuPc and the composite. The weight loss in both TNCuPc and composite observed in the TGA results are supported by the detection of endothermic peaks in the DSC results. These peaks appeared at about 360 °C for both MOF and composite, while TNCuPc registered the peak at about 450 °C. The melting peaks are observable owing to MOF decomposing completely to its precursors at high temperatures. These observations indicated that our materials did not directly decompose from the solid state as detected by endothermic peaks in DSC trace [44], which correspond to endothermic process.

The FE-SEM images of the synthesized TNCuPc and TNCuPc/MOF samples are given in Fig. 2a, c. The SEM image of TNCuPc (Fig. 2a)

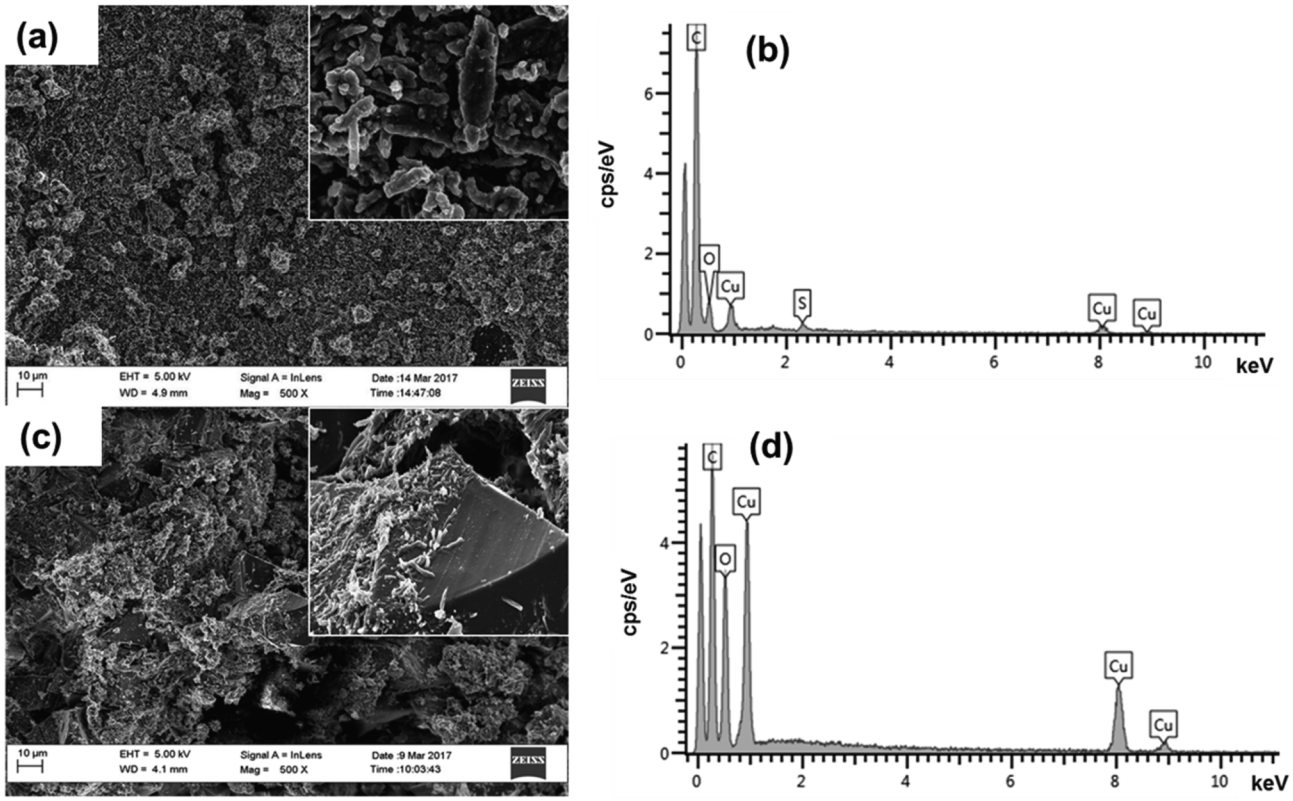

Fig. 2. SEM images of (a) TNCuPc, and (c) TNCuPc/MOF composite (inset: 5.00 kX magnification); and EDS results of (b) TNCuPc, and (d) TNCuPc/MOF composite.

shows rod shape-like structures [45–47]. The TNCuPc particles are dense with rod shape-like layers/structures stacked together due to dispersive forces and strong specific interactions between the surface groups on the Pc. On the other hand, TNCuPc/MOF composite shows some different surface features. It is interesting to note that the presence of TNCuPc crystals in the composite (Fig. 2c) exhibits some development of rod-like structures on the surface of the octahedral MOF. Furthermore, it can be seen that some of TNCuPc particles are attached on the surface, while others are entrenched in the frame structure. This suggests a possible interaction between MOF and TNCuPc as observed in XRD, UV–vis, and FTIR. In addition, The EDS analysis was performed for surface elemental composition based on the SEM images and presented in Fig. 2b, d, of TNCuPc and the composite, respectively and the supporting information in S1. This analysis revealed the presence of C-, O- and Cu- atoms as the elemental compositions in the composite. Nonetheless, the intensity of carbon in the composite is smaller than that of TNCuPc. This observation is quite surprising taking into account that the TNCuPc/MOF composite has higher content of both carbon and oxygen within its structure. The decrease in the peak intensity maybe attributable to a stronger interaction between the two components and the presence of substituted CuPc in the composite. This observation is also supported by the XRD results discussed (Fig. 1c), in which the crystallinity of the composite was affected by the presence of an amorphous TNCuPc.

Fig. 3a–c represents the TEM images of MOF, TNCuPc particles and TNCuPc/MOF composite. These figures show that both TNCuPc and MOF depict agglomerated spherical structures (Fig. 3a and b). When the composite was formed as depicted in Fig. 3c, the morphology was relatively tubular with some microporous structures still noticeable. These results show particles ranging in size between 50 and 150 nm, indicating that an impregnation method used in this study was able to develop nano-sized TNCuPc on the MOF structures. It has been reported that conjugated molecular systems obtained via intermolecular π–π interactions can form structures with various morphological structures [15,16]. The HR-TEM of MOF (Fig. 3d) showed that lattice fringes could be clearly observed and revealed a crystalline structure. The HR-TEM image of TNCuPc (Fig. 3e) presents a highly disordered structure without any sign of nanocrystals or ordered cluster formation, confirming a fully amorphous structure. In the case of the composite, the dark spots are observed as an indication of the presence of MOF upon composite formation (Fig. 3f). The corresponding SAED pattern (Fig. 3g) depicts multiple diffraction circles, indicating the polycrystalline feature of the MOF. This is in in good consent with the XRD results. The neat TNCuPc shown in (Fig. 3h) displayed no clear rings as an indicative amorphous state. Furthermore, the composite Fig. 3i retained the amorphous nature of the Pc, with further wrapping of MOF by TNCuPc as evidenced by both SEM and TEM studies. The EDX spectra (see Supporting Information) exhibit the presence of various elements in the synthesized MOF, TNCuPc and TNCuPc/MOF composite. The MOF structure (Fig. S2a, d) consists of Cu, C, and O due to the presence of organic linker and the metal. The TNCuPc structure (Fig. S2b, d) consists of Cu, C, and N due to the presence of phthalocyanine ring surrounding Cu. The internal mapping of the synthesized composite (Fig. S2c, d) shows Cu, C, O and N with a minimal reduction in the composition of C, which might be due to the interaction between TNCuPc and MOF. The presence of small peaks of Au and Si is attributed to the gold grid used during TEM analysis and some impurities, respectively.

The pore size and surface area are important parameters that have significant influence on gas adsorption properties. Fig. 4 shows the surface area and porosity obtained from N_2 adsorption analysis at 77 K. It can be seen in Fig. 4a that MOF clearly shows a Type-I isotherm with a small hysteresis loop at relative pressure from 0.81. This observation indicates the predominant microporous and mesoporous structures of such material based on the International Union of Pure and Applied Chemistry (IUPAC). The composite shows a similar Type-I isotherm and this is typically attributed to microporous materials [48]. Nonetheless, a small hysteresis is associated with the presence of some mesopores,

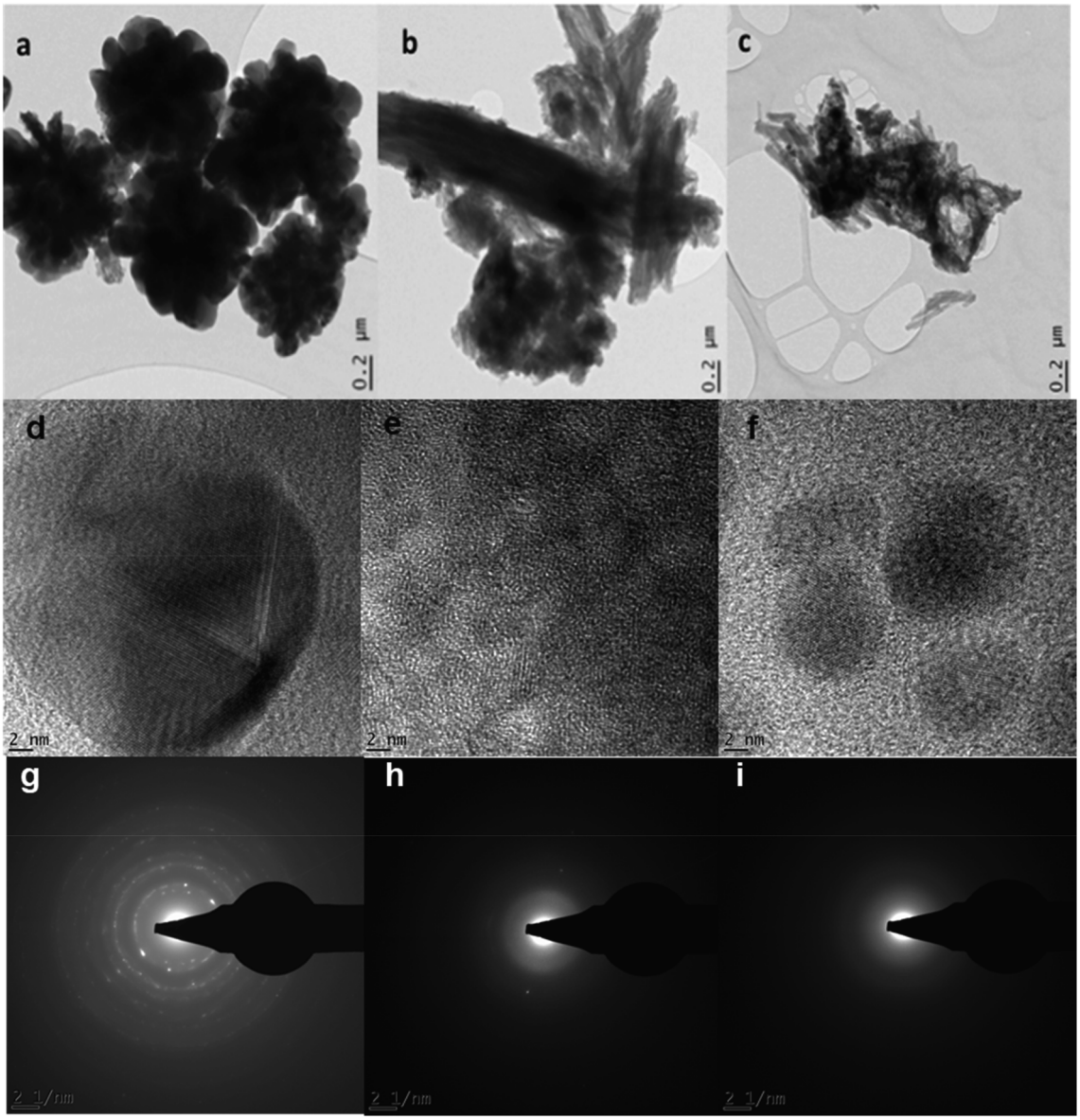

Fig. 3. TEM images of (a) MOF, (b) TNCuPc and (c) TNCuPc/MOF composite; HR-TEM images of (d) MOF, (e) TNCuPc and (f) TNCuPc/MOF composite; and SAED images of (g) MOF, (h) TNCuPc and (i) TNCuPc/MOF composite.

which decreases in the composite upon an introduction of TNCuPc particles. Furthemore, a more pronounced hysteresis loop for MOF (HKUST-1) decreasing with increasing the incorporation level was observed. The specific surface areas of MOF are 817.55, 614.67, and 514.93 $m^2.g^{-1}$ by Langmuir, BET and t-plot models, respectively (Table S1). These values are in closer range to those reported in the literature [49]. The TNCuPc exhibited a lower surface area values (Langmuir = 102.6 $m^2.g^{-1}$, BET = 73.9 $m^2.g^{-1}$ and t-plot = 3.48 $m^2.g^{-1}$), which also caused a decreased in the surface area values of the composite (273.16, 173.2, and 128.3 $m^2.g^{-1}$ by Langmuir, BET and t-plot models, respectively). Fig. 4b presents the pore volume of 8.82×10^{-2} $cm^3.g^{-1}$ and pore size of 76.9 Å obtained in MOF. The composite showed pore volume and pore size values of 5.96×10^{-2} cm^3/g and 157.9 Å, respectively. The reduction in surface area and pore volume of the composite maybe attributed to the introduction of TNCuPc with much lower porosity of 0.593×10^{-2} $cm^3.g^{-1}$. As seen in these results, a decrease in these parameters of the composite can be attributed to the number of factors such as reduction of the pore volume of the composite caused by the presence of nitro groups in phthalocyanine possessing a lower porosity, poor crystallinity of TNCuPc as evidenced by XRD results as well as TNCuPc agglomerates in the composite confirmed by SEM studies. This clearly caused an obvious reduction of the total pore volume of 0.109 $cm^3.g^{-1}$ in the composite in comparison to 0.312 $cm^3.g^{-1}$ of MOF.

CV studies

Cyclic voltammograms (CVs) were collected using Au electrode in 0.1 M TBAP/DMSO electrolytic solution to study the electrochemical properties of MOF, TNCuPc and TNCuPc/MOF composite. In this work, all the measured potentials against saturated Ag/AgCl electrode were converted to the reversible hydrogen electrode (RHE) scale according to the Nernst equation ($E_{RHE} = E_{Ag/AgCl} + 0.059\ pH + E^{o}_{Ag/AgCl}$, wherein $E^{o}_{Ag/AgCl} = 0.1976$ at 25 °C, and $E_{Ag/AgCl}$ is the experimentally measured potential against Ag/AgCl reference) [50]. The CVs are presented in Fig. 5a. It is noticeable that an introduction of 2×10^{-4} $mol.L^{-1}$ MOF in the electrolytic solution affected the reduction peak towards more negative potential as compared to blank. This observation is associated to the Cu

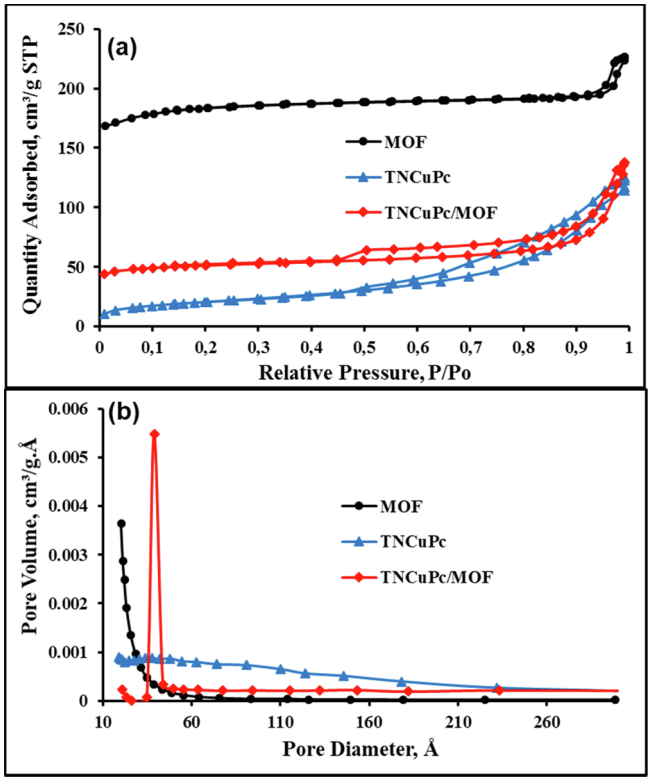

Fig. 4. (a) N_2 adsorption and (b) pore distribution curves of MOF, TNCuPc, and TNCuPc/MOF composite at 77 K.

deposition in MOF material involving two successive one-electron process [46]. The electrochemical reduction of Cu^{2+} in solution, which proceeds in two one-electron reversible waves via a Cu^{+} intermediate was due to the presence of ions in the solution [51]. However, this observation of the reduction of Cu^{2+} to Cu^{+} taking place at more negative potential can be attributed to electrochemical properties of Au electrode in an electrolytic system [33]. In the case of TNCuPc, two cathodic and anodic reversible peaks at around −1.4 and −0.34 V were observed. This observation agrees well with the reported literature for metal-free phthalocyanine and metallophthalocyanines [52,53]. These reductive peaks and one developed anodic peak can be plotted on multiscan voltammogram of TNCuPc as shown in Fig. 5c. It is well known that the centred Cu(II) and nitro groups at the periphery of metallophthalocyanine are redox-inactive possessing an electron withdrawal group, respectively [24]. Furthermore, the reduction couples are due to Pc ligands and these results are consistent with the reported literature of metal-free Pcs [52,53]. CV results of the composite exhibited both electrochemical characteristics of MOF and TNCuPc as an indicative of successful incorporation of MOF and TNCuPc. Multiscan CV characterisations of MOF, TNCuPc and TNCuPc/MOF were obtained in 0.1 M TBAP/DMSO system using Au working electrode at various scan rates ranging from 0.02 to 0.10 $V.s^{-1}$ and the results are presented in Fig. 5b-d. The multiscan voltammograms of MOF and TNCuPc show anodic–cathodic wave separations with increasing the scan rates. The TNCuPc/MOF composite given in Fig. 5d exhibits similar behaviour with increasing the scan rates. This observation indicates diffusion-controlled reactions on the surfaces of both TNCuPc and MOF structures [54].

To study the diffusion control characteristics of MOF, TNCuPc and TNCuPc/MOF composite, a plot of log current against the log scan rate was constructed and results are presented in Fig. 6a. From these results, a linear relationship was obtained for MOF, TNCuPc and TNCuPc/MOF composite with slopes of 0.433, 0.314 and 0.293, respectively. These observations show the characteristic of a response owing to diffusion transport of electron [55]. These observations were supported by the influence of a linear relationship of a decrease in peak current against the square root of scan rate plot as given in Fig. 6b, which suggests a semi-definite diffusion control mass transport [36].

Since all the multiscan voltammograms indicated a diffusion controlled process, the diffusion coefficient, D ($cm^2\ s^{-1}$) values were determined for electrocatalysts employing the plot of current versus the

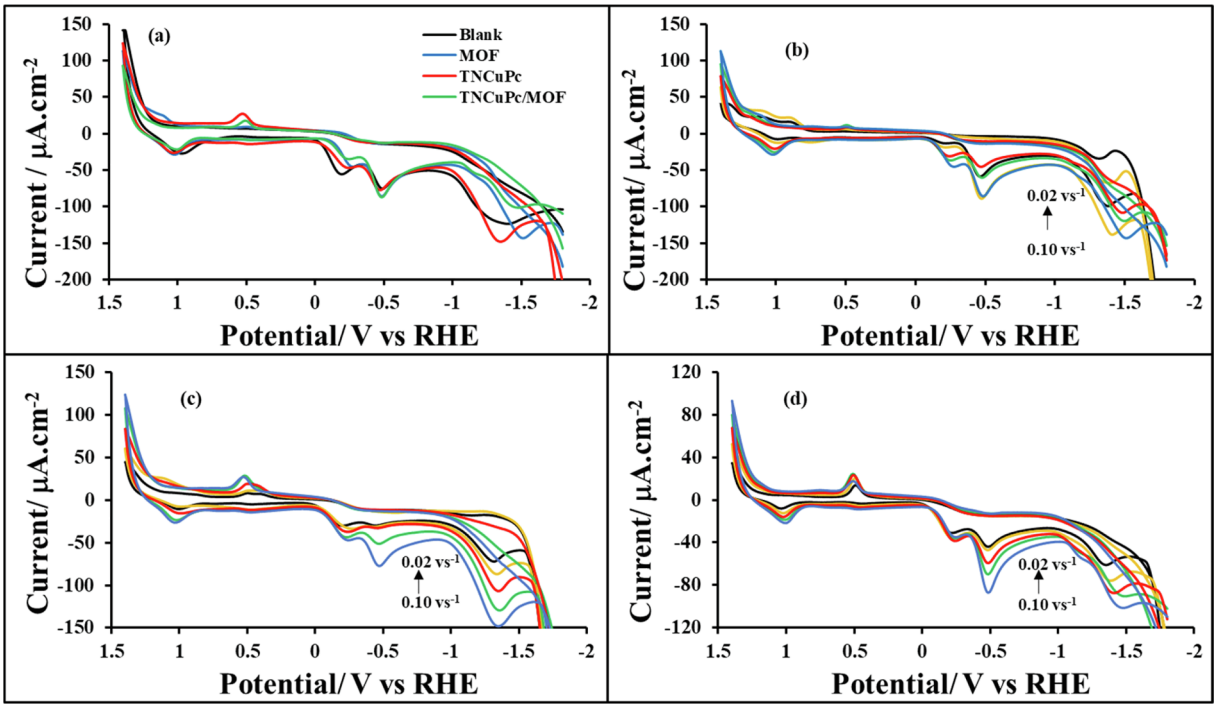

Fig. 5. (a) CV curves of MOF, TNCuPc and TNCuPc/MOF composite (~2.0×10^{-4} $mol.L^{-1}$) at 0.10 $V.s^{-1}$. The scan rate dependent CV curves of (b) MOF, (c) TNCuPc and TNCuPc/MOF solutions. The CVs plotted in (b) to (d) are for 0.02, 0.04, 0.06, 0.08 and 0.10 $V.s^{-1}$), starting from inside. Experimental condition: bare Au electrode and 0.1 M TBAP-DMSO.

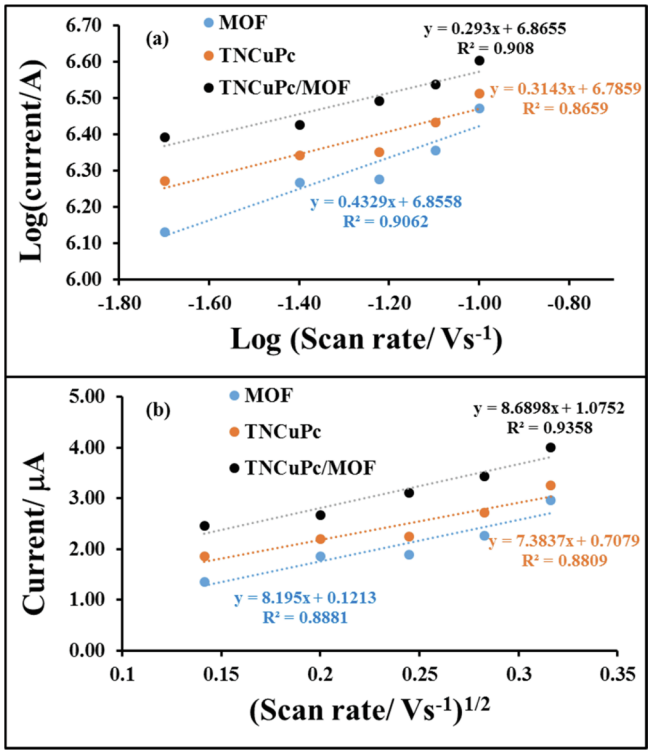

Fig. 6. (a) The log-log curves of the absolute value of the peak current against the scan rate and (b) Peak current vs square root of scan rate of MOF, TNCuPc and TNCuPc/MOF composite in an electrolytic solution at various scan rates, *v*, (0.02 – 0.10 Vs^{-1}).

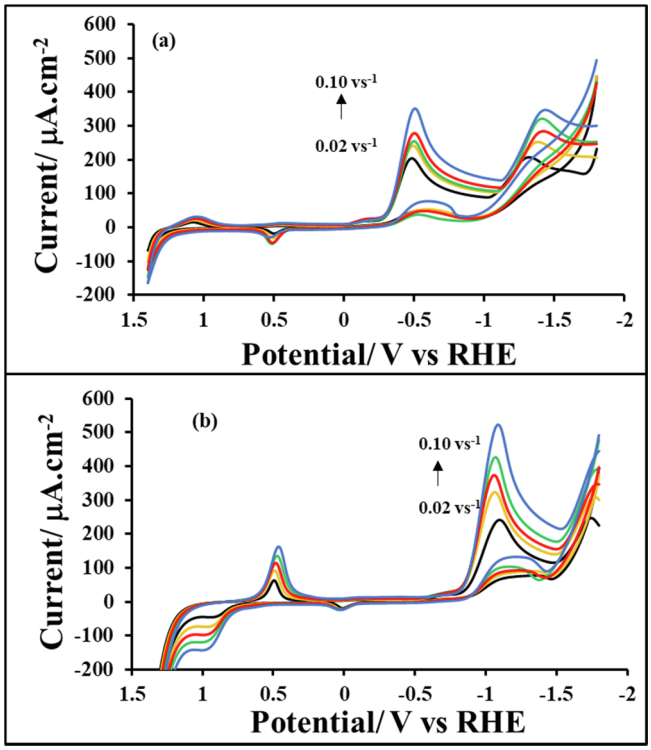

Fig. 7. CV curves of (a) TNCuPc and (b) TNCuPc/MOF composite (~2.0 × 10^{-4} mol.L^{-1}) at 0.10 Vs^{-1} and CV curves of various electrocatalysts in the presence 0.300 mol.L^{-1} H_2SO_4. The CVs plotted in (a) and (b) are for 0.02, 0.04, 0.06, 0.08 and 0.10 V s^{-1}), starting from inside. Experimental condition: bare Au electrode and 0.1 M TBAP/DMSO.

square root of the scan rates, $v^{1/2}$ and with the help of the Randles-Ševćik equation (Eq. (1)) for a quasi-reversible system [53]:

$$I_p = (2.65 \times 10^5) n^{3/2} A C D^{1/2} v^{1/2} \quad (1)$$

where *n* indicates the number of e- transferred, *A* is the area of electrode in cm^2, *C* is the bulk molar concentration of the electroactive species in mol.cm^{-3}. The diffusion coefficients found were 1.48 × 10^{-6}, 3.77 × 10^{-6} and 5.22 × 10^{-6} $cm^2.s^{-1}$ for MOF, TNCuPc and TNCuPc/MOF composite, respectively.

Electrochemical HER studies

The HER analysis (Fig. 7) of as-synthesized TNCuPc, and TNCuPc/MOF composite were examined in 0.300 mol.L^{-1} H_2SO_4 by CV measurement using 0.1 M TBAP/DMSO as a supporting electrolyte on a Au electrode. It was reported that a Au electrode exhibited some electrocatalytic HER properties with cathodic peak around −1.0 V vs RHE and this observation is in consistent with reports from other studies [33,54]. The HER properties can be due to non-polarizable (ability of an electrode to have charge transfer on the metal-electrolyte interface) nature of Au electrode. In order to evaluate HER activities of the synthesized materials, change in current density was used. An increase in current density shows that there is enhancement in the catalytic performance of the materials. Increase in the current density at the very same region upon introduction of MOF (Fig. S3) shows that MOF has ability to be used as an electrocatalyst. In the case of TNCuPc (Fig. 7a), the cathodic current response was higher as compared to MOF due to good electroconductive of phthalocyanine dye [24]. The voltammetric responses of TNCuPc/MOF composite (Fig. 7b), demonstrate a shift in HER wave towards more negative potentials as compared to MOF and TNcuPc. HER waves are important requirements of an electrocatalyst for HER [55]. Furthermore, the hydrogen activity of materials, *v* dependent studies were carried out using CV for TNCuPc and TNCuPc/MOF composite, respectively. After addition of hydrogen source (H_2SO_4), a shift in cathodic peaks of all the samples was observed at low potential, which shows that the amount of hydrogen produced was proportional to the *v* as seen in Fig. 7a, b. Furthermore, the increase in current was in line with the increase in the *v* as an indicative of the electrocatalytic property of the material. This is as an evident of semi-definite diffusion control mechanism [33]. This clearly tells that TNCuPc/MOF composite has a potential for conversion the hydrogen source to give high amounts of hydrogen development.

Furthermore, CV of TNCuPc and TNCuPc/MOF composite in the presence of H_2 source was carried out varying the H_2SO_4 concentration (0.033 – 0.450 mol.L^{-1}) in 0.1 mol.L^{-1} TBAP/DMSO electrolytic system and the results are depicted in Fig. 8a–c. It is noticeable that in both TNCuPc (Fig. 8a) and TNCuPc/MOF composite (Fig. 8b), the position of peaks dependents on the concentration of the H_2 source, whereby high cathodic current values are observed at low potential. Nonetheless, at lower concentration of the acid, the peak current of catalytic wave in MOF (Fig. S4) and TNCuPc/MOF (Fig. 8b) shows a direct relationship with the concentration, indicating an improvement in HER as given in Fig. 8c. In addition, the average catalytic rate constant was obtained from the slope of the plot of *I*pc against the concentration of the acid, and the results are shown in Fig. 8c inset. The results in this figure suggest that the process is the second-order in acid concentration [56].

It is well known that Tafel parameters (Tafel slopes, transfer coefficient and exchange current density) are used to evaluate HER processes for H_2 adsorption and desorption and illustrate the existence other effects such as kinetics [33,57–61]. These are crucial parameters of an electrode material. Figs. S5 and 9 represents polarization curves and linear Tafel plots (V versus log j_o plots) for TNCuPc, and TNCuPc/MOF materials. In an acidic media, mechanism for HER involves three important elementary steps [56-59]:

$H^+ + e^- + M \rightarrow MH_{ads}$ (Volmer)

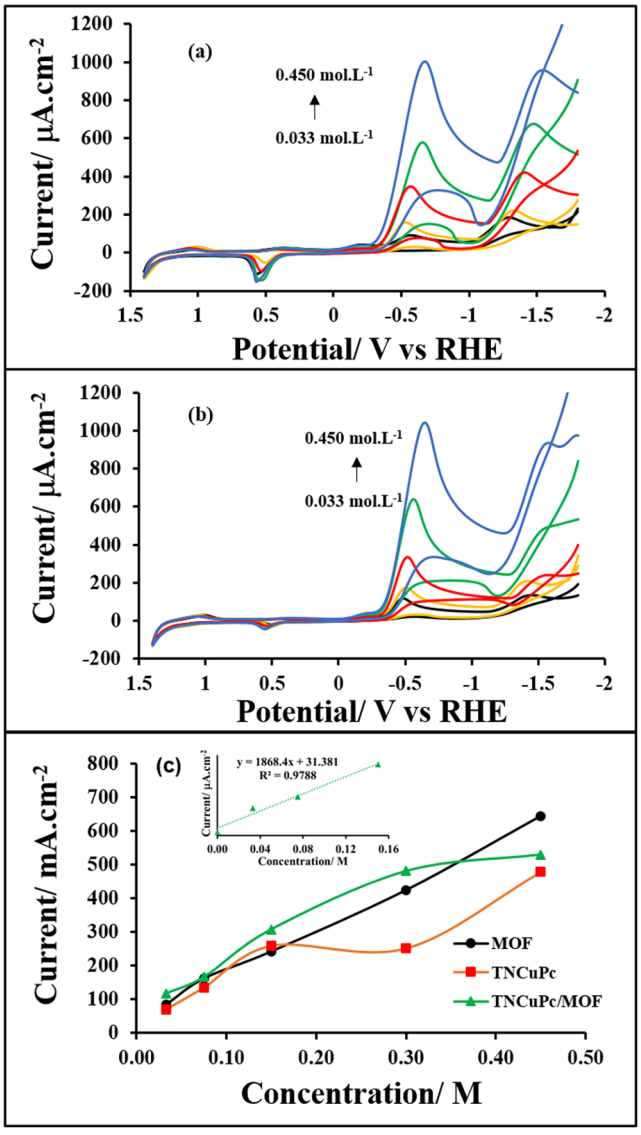

Fig. 8. CV curves of (a) TNCuPc and (b) TNCuPc/MOF composite ($\sim 2.0 \times 10^{-4}$ mol.L^{-1}) at different concentrations of H_2SO_4; and (c) current as a function of H_2SO_4 concentration of an electrocatalyst on bare Au electrode at fixed scan rate 0.10 Vs^{-1} and −0.648 V. Inset: Linear fitting of the composite.

$H^+ + MH_{ads} \rightarrow H_2$ (Heyrovsky)

$2MH_{ads} \rightarrow H_2$ (Tafel)

The Tafel parameters were estimated by linear fit of the polarization plots (Fig. 9, $\eta = b \log j_0 + a$), where b, represents the Tafel slope, j_0 is the exchange current density and cathodic transfer coefficient (α) and the results are given in Table 1. The α values were computed considering a high overpotential region, where the Butler–Volmer equation can be simplified to the Tafel equation. The b value is given by relationship ($(1-\alpha)F = -2.303RT$), where T – thermodynamic temperature (K), F – Faraday's constant given by 96,485C.mol^{-1} and R is the general gas constant (8.31451 J.mol^{-1}.K^{-1}).

From this study, the Tafel slope values obtained at 0.450 mol.L^{-1} were 213.5 mV.dec^{-1} (TNCuPc) and 163.6 mV.dec^{-1} (TNCuPc/MOF). It is noticeable that the composite gives a much smaller slope compared to the pristine MOF and TNCuPc electrocatalysts. Such high slopes are in agreement with what is reported in the literature on CPE/H-IL@Pd 10% (171.0 mV.dec^{-1}) and CPE (279 mV.dec^{-1}) [49]. These results suggest that both Heyvrosky (40 mV.dec^{-1}) or Tafel (30 mV.dec^{-1}) steps cannot be considered as rate determining steps (RDS) [52]. Therefore,

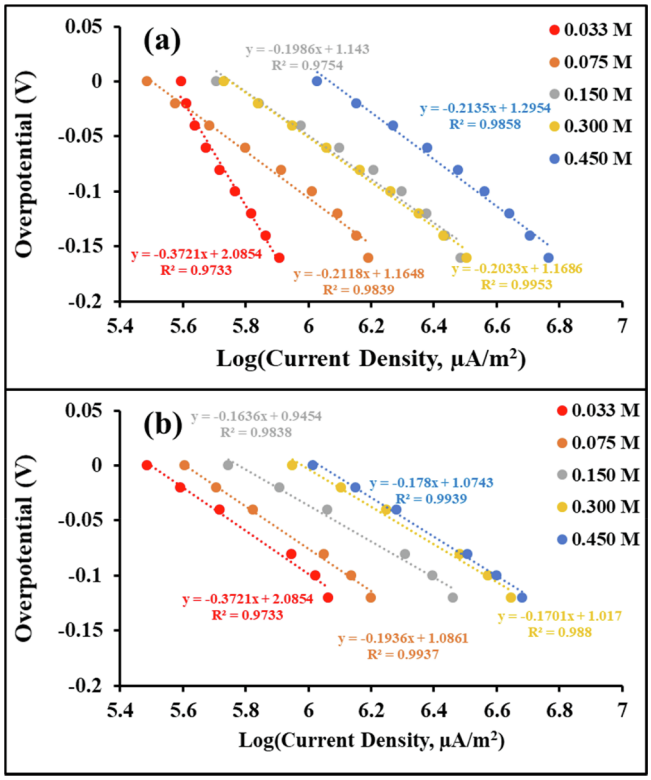

Fig. 9. Linear portion of Tafel plots of (a) TNCuPc and (b) TNCuPc/MOF composite in the presence of different H_2SO_4 concentration at 0.10 V.s^{-1} on Au electrode in an electrolytic system.

our results indicate that the Volmer reaction (adsorption of hydrogen proton on electrocatalyst surface) was the RDS despite higher Tafel slope values than expected (around 120 mV/dec) [26,33,54,57–59]. This observation was supported by α values (0.2778 and 0.3615 for TNCuPc and TNCuPc/MOF, respectively), which are all close to 0.5 [18,33,52,56,62]. In order to exhibit a clear understanding of the use of the as-prepared TNCuPc/MOF composite for catalytic usage, the proposed mechanism for HER is provided in Scheme 2. In the beginning, the H^+ adsorbs in the active site of composite forming [TNCuPc/MOF] H_{ads}. This step is known as Volmer. In Volmer-Heyrovsky mechanism, the adsorbed hydrogen proton combines with a proton from an electrolyte to form H_2, which means that the hydrogen desorption process was determined to be the electron chemical desorption [10]. Alternately, the two adsorbed neighbouring hydrogen atoms TNCuPc/MOF on the surface react with each other to give H_2 molecule (Volmer-Tafel mechanism) [7,8]. It is also noticeable that the i_o values increase with increasing the concentration of the acid. At 0.450 mol.L^{-1} H_2SO_4, the exchange current density values increase in the order of TNCuPc < TNCuPc/MOF composite. The large exchange current density observed in the TNCuPc/MOF composite indicates fast electron transfer rates. This is in agreement with the D values obtained.

Electrochemical impedance spectroscopy analysis

The electrochemical impedance spectroscopy (EIS) has gained popularity as an important electrochemical characterization technique that can measure and give response on the electrical resistance of several electrochemical systems. It is a powerful technique to divulge the conventional electrochemical measurements as well as to investigate the electrochemical kinetics of HER process [63]. The equivalent distributed resistance (EDR), consisting of both the equivalent series resistance (ESR) and the ionic resistance within the materials porous structure (i.e., RC semicircle), was obtained by extrapolating the

Table 1
The b, $(1–\alpha)$, and i_0 parameters of TNCuPc and TNCuPc/MOF composite.

Material	H_2SO_4 (mol.L^{-1})	b (V.dec^{-1})	$-b$ (mV.dec^{-1})	α	log j_o (μA.m^{-2})	j_o (μA.cm^{-2})
TNCuPc	0.033	−0.3721	372.1	0.1589	5.59	39.2
	0.075	−0.2118	211.8	0.2792	5.49	30.6
	0.150	−0.1986	198.6	0.2978	5.71	50.8
	0.300	−0.2033	203.3	0.2909	5.73	53.7
	0.450	−0.2135	213.5	0.2770	6.03	106.5
TNCuPc/MOF	0.033	−0.3721	372.1	0.1589	5.49	30.6
	0.075	−0.1936	193.6	0.3055	5.60	40.2
	0.150	−0.1636	163.6	0.3615	5.74	55.5
	0.300	−0.1913	191.3	0.3091	5.95	88.9
	0.450	−0.1636	163.6	0.3615	6.01	103.3
Pd@CuPc/MOF [18]	0.300	−0.1770	177.0	0.3341	[a]	[a]
CuPc/MOF [62]	0.300	−0.1595	159.5	0.3708	[a]	[a]
PABA/MOF [33]	0.300	−0.1305	130.5	0.4500	[a]	[a]
MOF-3 wt%-PABA [56]	0.300	−0.1667	166.7	0.3550	[a]	[a]
MOF-5 wt%-PABA [56]	0.300	−0.1535	153.5	0.3850	[a]	[a]
PANI/MOF [51]	0.300	−0.1993	199.3	0.297	[a]	[a]

[a] log j_0 and j_0 are in different units as compared to the one in this work.

vertical portion of the plot to the real axis. Fig. 10 presents the overlaid Nyquist plots of a blank, MOF, TNCuPc and TNCuPc/MOF composite in 0.1 M TBAP/DMSO electrolyte, (a) without and with (b) 0.45 mol.L^{-1} H_2SO_4, studied under open circuit potential (OCP) with the frequency range 5×10^5 Hz − 0.7 Hz. The Nyquist plots were fitted with the electrical equivalent circuit (EEC), which comprises of Voigt RC elements, involving a solution/electrolyte resistance (R_s denoted as R1), charge-transfer resistance (R_{ct} denoted as R2) and constant phase elements (CPE or Q) as shown by inset of Fig. 10a. The diameter of the semicircle of Nyquist plot provides charge transfer resistance (R_{ct}) of the interface, and its value is obtained by fitting the EEC. As observed in Fig. 10a, the semicircle for TNCuPc/MOF composite is smaller than blank and MOF, which could be the reason for enhanced electrochemical properties caused by TNCuPc. Fig. 10b presents the Nyquist plot of the EIS response for blank, MOF, TNCuPc and TNCuPc/MOF composite in 0.1 M TBAP/DMSO mixed with 0.45 M H_2SO_4 as electrolyte. The small semicircle was observed in all materials as compared to Fig. 10a without acid. It was reported that the radius of high frequency semicircle reveals hydrogen absorption and low frequency semicircle represents the HER kinetics [63,64]. As seen in Fig. 10(b), the R_{ct} for TNCuPc/MOF composite is smaller. than MOF and TNCuPc value as shown in Table 2 (i.e., from 41. kΩ to 12.6 kΩ), demonstrating the excellent conductivity of the composites. The R_{ct} value for the composite is closed to the one reported by Nivetha and Grace [64]. R_{ct} of materials follow the sequence of blank < MOF < TNCuPc < TNCuPc/MOF. Accordingly, a small semicircle designates a high HER activity with a small Rct value for the TNCuPc/MOF composite. Furthermore, EIS results show a reduced charge transfer resistance and improved conductivity because of the presence of TNCuPc support. On the other hand, the constant phase element (CPE or C2) was determined to evaluate the exposed active surface area of the electrode. As shown in Table 2, TNCuPc/MOF exhibits the largest CPE compared to MOF and TNCuPc. Thus, these findings advocate that the synthesized TNCuPc/MOF composite is a promising electrocatalyst for hydrogen evolution reaction.

Conclusions

In summary, we have successfully developed a hybrid-hybrid TNCuPc/MOF composite derived from MOF embraced in TNCuPc through impregnation method. The as-prepared TNCuPc/MOF composite was used as an efficient electrocatalyst for HER process in an acidic medium. The composite showed excellent catalytic action and exceptional stability for HER in acidic medium. It was demonstrated that the electrocatalytic activity of the TNCuPc/MOF composite was higher as compared to the neat MOF. The observed positive roles of incorporated

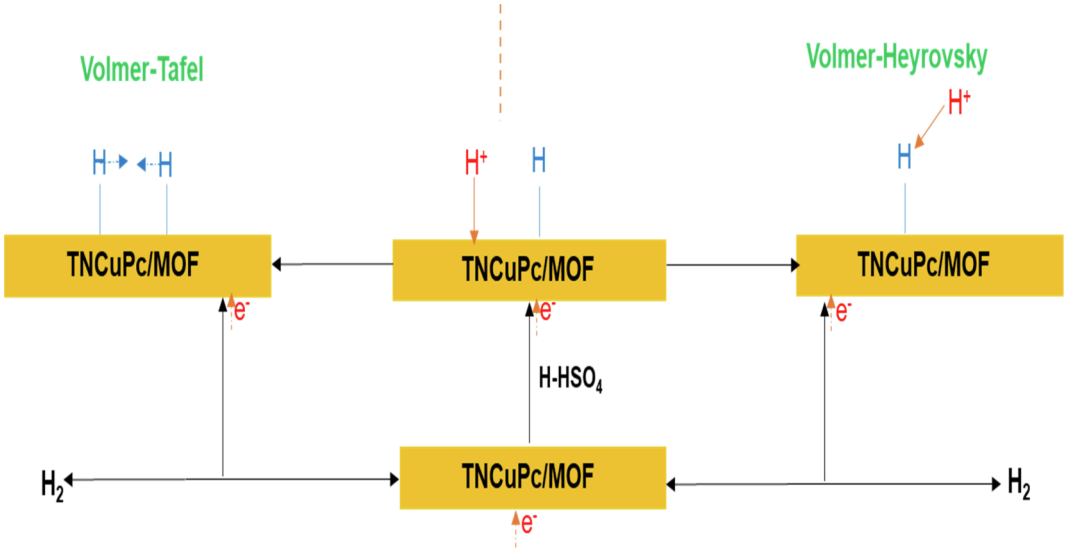

Scheme 2. HER mechanism for (~2.0 $\times 10^{-4}$ mol.L^{-1}) of TNCuPc/MOF composite at 0.10 V.s^{-1} in the concentration of 0.450 mol.L^{-1} H_2SO_4.

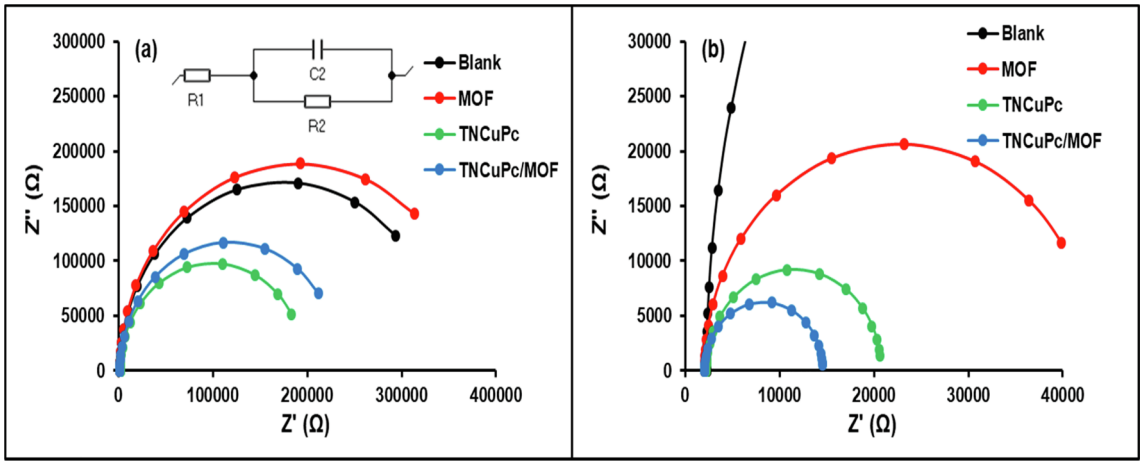

Fig. 10. Nyquist plots of the Blank, MOF, TNCuPc, TNCuPc/MOF composite in 0.1 M TBAP/DMSO electrolyte at OCP with the frequency range 5.0×10^5 Hz-0.7 Hz, (a) without and with (b) 0.45 mol.L^{-1} H_2SO_4.

Table 2
Fitted circuit parameters of EIS for blank, MOF, TNCuPc and TNCuPc/MOF composite.

Material	Electrolyte	R_s (kΩ)	CPE (μF)	R_{ct} (kΩ)
Blank	TBAP-DMSO	1.00	0.100	0.100
	TBAP-DMSO/H_2SO_4	2.27	0.634	223
MOF	TBAP-DMSO	1.60	0.276	377
	TBAP-DMSO/H_2SO_4	2.06	1.152	41.4
TNCuPc	TBAP-DMSO	2.00	0.330	196
	TBAP-DMSO/H_2SO_4	2.26	0.090	18.5
TNCuPc/MOF	TBAP-DMSO	1.62	0.326	234
	TBAP-DMSO/H_2SO_4	2.04	0.727	12.6

TNCuPc in the composite was attributed to possible synergetic effects between TNCuPc crystals and the MOF, resulting to a facilitation of HER process as part of hydrogen production. Furthermore, the Tafel slopes and charge transfer coefficients exhibited that the rate-determining step for HER on the studied samples maybe the Volmer coupled with Heyrovsky reaction or Tafel reaction. The exceptional performance for HER can be ascribed to the distinctive TNCuPc architecture with robust contact between the TNCuPc and MOF, as well as plentiful active reaction sites. The EIS results also supported Tafel analyses with improved CPE and R_{ct} values. This study affords a route to prepare a MOF based composite electrocatalyst with high efficiency and tremendous electrocatalytic activity for HER.

Acknowledgements

MJ Hato and KD Modibane greatly appreciate the National Research Foundation (NRF) under Thuthuka programme (UID Nos. 117727 and 118113) and University of Limpopo (Project Nos. R202 and R232), South Africa for financial supports. Sasol Foundation of South Africa is highly appreciated for purchasing both STA and UV-vis instruments. Hato would like to pass his greatest appreciation to Prof Masahiro Yoshimura (National Cheng Kung University, Taiwan) for his prolific discussion during the IUMRS-ICAM 2017.

Author contributions

MJ Hato, KD Modibane, KM Molapo and EI Iwuoha conceived and designed the experiments; GR Monama, KE Ramohlola and TC Maponya synthesized all the samples and evaluated their morphology, crystalline structure and chemical composition. Hato and Modibane evaluated the thermal analyses of the prepared samples; SB Mdluli helped with characterization of the samples using cyclic voltammetry. DM Teffu ran the EIS analysis. Hato, Molapo, K Makgopa, Iwuoha and Modibane discussed EIS and hydrogen studies. Hato, Molapo, Modibane and Monama wrote the initial manuscript. All the authors contributed to the final approval of the version of the manuscript to be submitted.

Appendix A. Supplementary data

Supplementary data to this article can be found online at https://doi.org/10.1016/j.rinp.2019.102564.

References

[1] Eftekhari A. Electrocatalysts for hydrogen evolution reaction. Int J Hydrogen Energy 2017;42:11053–77.
[2] Zhang L, Chang Q, Chen H, Shao M. Recent advances in palladium-based electrocatalysts for fuel cell reactions and hydrogen evolution reaction. Nano Energy 2016;29:198–219.
[3] Zhang Z, Tang H, Cheng D, Zhang J, Chen Y, Shen X, et al. Strain coupling and dynamic relaxation in multiferroic metal-organic framework $[(CH_3)_2NH_2][Mn(HCOO)_3]$ with perovskite structure. Res Phys 2019;12:2183–8.
[4] Zheng J. Seawater splitting for high-efficiency hydrogen evolution by alloyed $PtNi_x$ electrocatalysts. Appl Surf Sci 2017;413:360–5.
[5] Hod I, Deria P, Bury W, Mondloch JE, Kung CW, So M, et al. A porous proton-relaying metal-organic framework material that accelerates electrochemical hydrogen evolution. Nat Commun 2015;6:8304–12.
[6] Voiry D, Salehi M, Silva R, Fujita T, Chen M, Asefa T, et al. Conducting MoS_2 nanosheets as catalysts for hydrogen evolution reaction. Nano Lett 2013;13:6222–7.
[7] Zheng J, Jiao ZZ. Modified Bi2WO6 with metal-organic frameworks for enhanced photocatalytic activity under visible light. J Colloid Interface Sci 2017;488:234–9.
[8] Ren Y, Chia GH, Gao Z. Metal-organic frameworks in fuel cell technologies. Nano Today 2013;8:577–97.
[9] Satyapal S, Petrovic J, Read C, Thomas G, Ordaz G, The US. Department of Energy's National Hydrogen Project: Progress towards meeting hydrogen-powered vehicle requirements. Catal Today 2017;120:246–56.
[10] Su W, Wang P, Cai Z, Yang J, Wang X. One-pot hydrothermal synthesis of Al-doped MoS_2@graphene aerogel nanocomposite electrocatalysts for enhanced hydrogen evolution reaction. Res Phys 2019;12:250–8.
[11] Yin X, Yan Y, Miao M, Zhan K, Li P, Yang J. Quasi-emulsion confined synthesis of edge-rich ultrathin MoS_2 nanosheets/graphene hybrid for enhanced hydrogen evolution. Chemistry 2018;24:556–60.
[12] Mashao G, Ramohlola KE, Mdluli SB, Monama GR, Hato MJ, Makgopa K, et al. Zinc-based zeolitic benzimidazolate framework/polyaniline nanocomposite for electrochemical sensing of hydrogen gas. Mater Chem Phys 2019;230:287–98.
[13] Liu W, Yin X-B. Metal-organic frameworks for electrochemical applications. TrAC Trends in Anal Chem 2016;75:86–96.
[14] Lee C-H, Filler R, Lee JY, Li J, Mandal BK. Synthesis and hydrogen adsorption properties of a new phthalocyanine-based metal-organic framework. Renew Energy 2010;35:1592–5.
[15] Koca A. Copper phthalocyanine complex as electrocatalyst for hydrogen evolution reaction. Electrochem Commun 2009;11:838–41.
[16] Sleven J, Walrand CG, Binnemans K. Synthesis, spectral and mesomorphic properties of octa-alkoxy substituted phthalocyanine ligands and lanthanide complexes. Mater Sci Eng C 2001;18:229–38.
[17] Li T, Tang D, Cui Z, Cai B, Li D, Chen Q, et al. Functionalised carbon nanotubes for highly active and metal-free electrocatalysts in hydrogen evolution reaction. Electrocatalysis 2018;9:573–81.

[18] Monama GR, Mdluli SB, Mashao G, Makhafola MD, Ramohlola KE, Molapo KM, et al. Palladium deposition on copper(II) phthalocyanine/metal organic framework composite and electrocatalytic activity of the modified electrode towards the hydrogen evolution reaction. Renew Energy 2018;119:62–72.
[19] Franceschini EA, Lacconi GI. Synthesis and performance of nickel/reduced graphene oxide hybrid for hydrogen evolution reaction. Electrocatalysis 2018;9:47–58.
[20] Ziminov AV, Polevaya YA, Jourre TA, Ramsh SM, Mezdrogina MM, Poletaev NK. Photoluminiscence of nitro-substituted europium (III) phthalocyanines. Semiconductors 2010;44:1070–3.
[21] Ai L, Zhang C, Li L, Jiang J. Iron terephthalate metal-organic framework: revealing the effective activation of hydrogen peroxide for the degradation of organic dye under visible light irradiation. Appl Catal B Environ 2014;148–149:191–200.
[22] Mphuthi NG, Adekunle AS, Fayemi OE, Olasunkanmi LO, Ebenso EE. Phthalocyanine doped metal oxide nanoparticles on multiwalled carbon nanotubes platform for the detection of dopamine. Sci Rep 2017;7:43181–202.
[23] Kumar RS, Kumar SS, Kulandainathan MA. Highly selective electrichemical reduction of carbon dioxide using Cu based metal organic framework as an electrocatalyst. Electrochem Commun 2012;25:70–3.
[24] Cong F-D, Ning B, Yu HF, Cui XJ, Chen B, Cao SG, et al. the control of phthalocyanine properties through nitro-group electronic effect. Spectrochim Acta – Part A Mol Biomol Spectrosc 2005;62:394–7.
[25] Litrán R, Blanco E, Ramírez-Del-Solar M, Esquivias L. Trapping copper phthalocyanine in a silica sono-xerogel. J Sol-Gel Sci Technol 1997;8:985–90.
[26] Leznoff CC, McKeown NB. Preparation of substituted tetrabenzontriazaporphyrins and a tetranaphthotriazaporphyrin: a route to mono-meso-substituted phthalocyanine analogs. J Org Chem 1990;55:2186–90.
[27] Loera-Serna S, Oliver-Tolentino MA, de Lourdes López-Núñez M, Santana-Cruz A, Guzmán-Vargas A, Cabrera-Sierra R, et al. Electrochemical behavior of $[Cu_3(BTC)_2]$ metal-organic framework: The effect of the method of synthesis. J Alloys Compd 2012;540:113–20.
[28] Albay C, Koç M, Altin I, Bayrak R, Değirmencioğlu I, Sökmen M. New dye sensitized photocatalysts: Copper(II)-phthalocyanine/TiO_2 nanocomposite for water remediation. J Photochem Photobiol A Chem 2016;324:117–25.
[29] Abbasi AR, Karimi MM, Daasbjerg K. Efficient removal of crystal violet and methylene blue from wastewater by ultrasound nanopartciles Cu-MOF in comparison with mechanosynthesis method. Ultrason Sonochemistry 2017;37:182–91.
[30] El-Nahass MM, Abd-El-Rahman KF, Darwish AAA. Fourier-transform infrared and UV-vis spectroscopes of nickel phthalocyanine thin films. Mater Chem Phys 2005;92:185–9.
[31] Seoudi R, El-Bahy GS, El Sayed ZA. FTIR, TGA and DC elctrical conductivity studies of phthalocyanine and its complexes. J Mol Struct 2005;753:119–26.
[32] Zhang M, Shao C, Guo Z, Zhang Z, Mu J, Cao T, et al. Hierarchical nanostructures of copper(II) phthalocyanine on electronspun TiO_2 nanofibers: controllable solvothermal-fabrication and enhanced visible photocatalytic properties. ACS Appl Mater Interfaces 2011;3:369–77.
[33] Ramohlola KE, Masikini M, Mdluli SB, Monama GR, Hato MJ, Molapo KM, et al. Electrocatalytic hydrogen production properties of poly(3-aminobenzoic acid) doped with metal organic frameworks. Int J Electrochem Sci 2017;12:4392–405.
[34] Kung CW, Chang TH, Chou LY, Hupp JT, Farha OK, Ho KC. Porphyrin-based metal-organic framework thin films for electrochemical nitride detection. Electrochem Commun 2015;58:51–6.
[35] Zhao SN, Song XZ, Song SY, Zhang H. Highly efficient heterogeneous catalytic materials derived from metal-organic framework supports/precursors. Coord Chem Rev 2017;337:80–96.
[36] Guo H, Zhang Y, Zheng Z, Lin H, Zhang Y. Facile one-pot fabrication of Ag@MOF (Ag) nanocomposites for highly selective detection of 2,4,6-trinitrophenol in aqueous phase. Talanta 2017;170:146–51.
[37] Chen H, Wang L, Yang J, Yang RT. Investigation on hydrogenation of metal-organic frameworks HKUST-1 MIL-53, and ZIF-8 by hydrogen spillover. J Phys Chem C 2013;117:7565–76.
[38] Wan Y, Chen S, Wang G, Liang Q, Li Z, Xu S. Facile synthesis and characterization of zinc tetranitro phthalocyaanine-MWNCTs nanocomposites with efficient visible-light-driven. Acta Phys Pol A 2016;130:785–90.
[39] Zongo S, Dhlamini MS, Neethling PH, Yao A, Maaza M, Sahraoui B. Synthesis, characterization and femtosecond nonlinear saturable absorption behavior of copper phthalocyanine nanocrytals doped-PMMA polymer thin films. Opt Mater (Amst) 2015;50:138–43.
[40] Zhao Y, Cao Y, Zhong Q. CO_2 capture on metal organic framework and graphene oxide composite using a high pressure static adsorption apparatus. J Clean Energy Technol 2014;2:24–7.
[41] Reza A, Karimi M, Daasbjerg K. Efficient removal of crystal violet and methylene blue from wastewater by ultrasound nanoparticles Cu-MOF in comparison with mechanosynthesis method. Ultrason Sonochem 2017;37:182–91.
[42] Lin K-S, Adhikari AK, Ku C-N, Chiang C-L, Kuo H. Synthesis and characterization of porous KHUST-1 metal organic frameworks for hydrogen storage. Int J Hydrogen Energy 2012;37:13865–71.
[43] Fleker O, Borenstein A, Lavi R, Benisvy L, Ruthstein S, Aurbach D. Preparation and properties of metal organic framework/activated carbon composite materials. Langmuir 2016;32:4935–44.
[44] Kim KJ, Li YJ, Kreider PB, Chang CH, Wannenmacher N, Thallapally PK, et al. High-rate synthesis of Cu-BTC metal-organic frameworks. Chem Commu 2013;49:11518–20.
[45] Walter MG, Rudine AB, Wamser CC. Porphyrins and phthalocyanines in solar photovoltaics cells. J Porphyr Phthalocyanines 2010;14:759–92.
[46] Raoof JB, Hosseini SR, Ojani R, Mandegarzad S. MOF-derived Cu/nanoporous carbon composite and its application for electro-catalysis of hydrogen evolution reaction. Energy 2015;90:1075–81.
[47] Ge S, Zhang Y, Huang B, Huang S, Tie W, Lei Y. Synthesis of highly crystalline copper phthalocyanine needles by solvothermal method. Mater Lett 2016;163:61–4.
[48] Pakapongpan S, Mensing JP, Phokharatkul D, Lomas T. Highly selective electrochemical sensor for ascorbic acid based on a novel hybrid graphene-copper phthalocyanine-polyaniline nanocomposites. Electrochim Acta 2014;133:294–301.
[49] Lin J, Hassan M, Bo XX, Guo L. Synthesis of iron-based metal-organic framework@large mesoporous carbon composites and their electrocatalytic properties. J Electrochem Chem 2017;801:373–80.
[50] Wang L, Lee CY, Schmuki P. Solar water splitting: preserving the beneficial small feature size in porous α-Fe_2O_3 photoelectrodes during annealing. J Mater Chem A 2013;1:212–5.
[51] Ramohlola KE, Monana GR, Hato MJ, Modibane KD, Molapo KM, Masikini M, et al. Electrocatalytic hydrogen evolution reaction of polyaniline-metal organic framework nanocomposite. Compos B: Eng 2018;137:129–39.
[52] Nila C, González I. Thermodynamics of $CuH_2SO_4Cl^-H_2O$ and $CuNH_4ClH_2O$ based on predominance-existance diagrams and Pourbaix-type diagrams. Hydrometallurgy 1996;42:63–72.
[53] Esenpınar AA, Özkaya AR, Bulut M. Synthesis and electrochemical properties of crown ether functionalized coumarin substituted cobalt and copper phthalocyanines. J Organomet Chem 2011;696:3873–81.
[54] Nakşi M, Cihan A. Synthesis and electrochemical properties of phthalocyanines with four 8-quinolinoxy-substituents. Transit Met Chem 2005;30:89–94.
[55] Xu Z, Li K, Hu H, Zang Q, Cao L, Li J, et al. From bulk to nano metla phthalocyanine by recrystallization with enhanced nucleation. Dyes Pigm 2017;139:97–101.
[56] Ramohlola KE, Masikini M, Mdluli SB, Monama GR, Hato MJ, Molapo KM, et al. Electrocatalytic hydrogen evolution reaction of metal organic frameworks decorated with poly(3-aminobenzoic acid). Electrochim Acta 2017;246:1174–82.
[57] Chen J, Xia G, Jiang P, Yang Y, Li R, Shi R, et al. Active and durable hydrogen evolution reaction catalyst derived from Pd-doped metal-organic frameworks. ACS Appl Mater Interfaces 2016;8:13378–83.
[58] Zhou H, Zhang J, Zhang J, Yan XF, Shen XP, Yuan A-H. Spillover enhanced hydrogen storage in Pt-doped MOF/graphene oxide composite produced via an impregnation method. Inorg Chem Commun 2015;54:54–6.
[59] Boomi P, Prabu HG, Mathiyarasu J. Synthesis and characterization of polyaniline/Ag-Pt nanocomposite for improved antibacterial. Colloids Surf B: Biointerfaces 2013;103:9–14.
[60] Wu C, Li C, Yang B, Zhou S, Shi D, Wang Y, et al. Electrospun MnCo2O4 nanofibers for efficient hydrogen evolution reaction. Mater Res Express 2016;3:095018.
[61] Zhou W, Jia J, Lu J, Yang L, Hou D, Li G, et al. Recent developments of carbon-based electrocatalysts for hydrogen evolution reaction. Nano Energy 2016;28:29–43.
[62] Monama GR, Modibane KD, Ramohlola KE, Molapo KM, Hato MJ, Makhafola MD, et al. Copper(II) phthalocyanine/metal organic framework electrocatalyst for hydrogen evolutionreaction application. Int J Hydrogen Energy 2019;44:18891–902.
[63] Tang Y-J, Wang Y, Wang X-L, Li S-L, Hunag W, Dong L-Z, et al. Molybdenum disulfide/nitrogen-doped reduced graphene oxide nanocomposite with enlarged interlayer spacing for electrocatalytic hydrogen evolution. Adv Energy Mater 2016;6:1600116–22.
[64] Nivetha R, Grace AN. Manganese and zinc ferrite based graphene nanocomposites for electrochemical hydrogen evolution reaction. J Alloys and Compds 2019;796:185–95.